



ISTITUTO NAZIONALE DI RICERCA METROLOGICA Repository Istituzionale

Characterization and assessment of the wideband magnetic properties of nanocrystalline alloys and soft ferrites

This is the author's submitted version of the contribution published as:

Original

Characterization and assessment of the wideband magnetic properties of nanocrystalline alloys and soft ferrites / Ferrara, Enzo; Fiorillo, Fausto; Beatrice, Cinzia; Dobák, Samuel; Ragusa, Carlo; Magni, Alessandro; Appino, Carlo. - In: JOURNAL OF MATERIALS RESEARCH. - ISSN 0884-2914. - 33:15(2018), pp. 2120-2137. [10.1557/jmr.2018.275]

Availability:

This version is available at: 11696/59711 since: 2021-01-28T14:45:14Z

Publisher:

Cambridge University Press

Published

DOI:10.1557/jmr.2018.275

Terms of use:

This article is made available under terms and conditions as specified in the corresponding bibliographic description in the repository

Publisher copyright

(Article begins on next page)

Characterization and assessment of the wideband magnetic properties of nanocrystalline alloys and soft ferrites.

Enzo Ferrara^{1*}, Fausto Fiorillo¹, Cinzia Beatrice¹, Samuel Dobák³, Carlo Ragusa², Alessandro Magni¹, Carlo Appino¹

¹Istituto Nazionale di Ricerca Metrologica INRIM, Torino, Italy

²Energy Department, Politecnico di Torino, Torino, Italy.

³Institute of Physics, P.J. Šafárik University, Košice, Slovakia.

Abstract— Efficient applications of magnetic cores in sensing and power electronics require low-loss and versatile soft magnetic materials, with excellent response on a wide range of frequencies. This objective is traditionally pursued with ferrite and permalloy tape cores, available under a variety of properties. Comparable and even superior soft magnetic behavior can, however, be obtained on amorphous and nanocrystalline alloys, with the latter, in particular, combining flexible response to the thermal treatments with high magnetic saturation. Broadband precise magnetic characterization of these materials, crucial to their use as inductive cores, is fully appreciated when associated with assessment by physical modeling. Comprehensive measuring approach and significant results obtained in sintered soft ferrites and nanocrystalline ribbons up to 1 GHz are highlighted in this paper. We show how broadband loss and permeability behaviors can be quantitatively interpreted in the framework of the loss separation concept, applied to eddy current and spin damping dissipation mechanisms.

Index Terms — Soft ferrites, Nanocrystalline alloys, Magnetic losses, Wideband magnetic measurements, Loss models.

Corresponding author: E. Ferrara, INRIM, e.ferrara@inrim.it

1. Introduction

The soft magnetic materials nowadays available to industry are required to cover a tremendous array of applications, from the classical use as cores of transformers, generators, and motors, to the great variety of inductive components employed in power electronics, sensing, automotive, household, recording, telecommunication technologies. Remarkably, all these functions are covered with a handful of compositions, providing the best compromise among a number of requirements, of which the excellent soft magnetic behavior is not always the most important one. A vast and expanding applicative area for soft magnetic cores concerns a multitude of devices for electronics, which call for soft magnetic materials endowed with high permeability and low losses over a broad range of frequencies, from DC to several MHz. Relevant examples of applications are found in the switch-mode power supply (SMPS), converters, inverters, radio-frequency interference filters, and magnetic amplifiers, where the core losses and the ensuing temperature rise are main issues. Soft ferrites have traditionally dominated this field of applications. They are mixed oxides, having the general composition $MO \cdot Fe_2O_3$, where M is a divalent metal ion such as Fe^{2+} , Mn^{2+} , Ni^{2+} , Zn^{2+} , Mg^{2+} . The Mn-Zn and Ni-Zn ferrite cores, obtained by sintering the oxide powders, are the standard industrial products, with the Ni-Zn types covering a broader frequency range, typically up to some 10 MHz versus a typical 1 MHz limit of Mn-Zn ferrites, at the cost of reduced permeability [1]. The key to the soft magnetic properties of ferrites is the so-called mechanism of “anisotropy compensation” [2], where the negative magnetocrystalline anisotropy of the Fe^{3+} ions is compensated by the positive anisotropy of divalent cations, like Fe^{2+} or Co^{2+} , introduced on purpose. With suitable concentration of these ions, the resultant anisotropy constant will cross the zero value at a convenient temperature (typically, between room temperature and 100 °C). Full anisotropy compensation is, for example, obtained at 300K with the composition $Mn_{0.53}Zn_{0.40}Fe_{0.07}Fe_2^{3+}O_4$. It is easily understood that vanishing magnetic anisotropy opens the way to soft and extra-soft magnetic properties, because the magnetization process, be it accomplished by domain wall (dw) displacements or the rotation of the magnetic moments, is the easier the lower is the anisotropy energy (i.e the anisotropy constant K). A simplified approach to the coercive field H_c and the initial permeabilities by dw motion μ_i^{dw} and rotations μ_i^{rot} provides

$$H_c \propto \frac{K^{1/2}}{J_s \langle s \rangle}, \quad \mu_i^{dw} \propto \frac{J_s^2 \cdot \langle s \rangle}{K^{1/2}}, \quad \mu_i^{rot} \propto \frac{J_s^2}{K}, \quad (1)$$

in a material of saturation polarization J_s and average grain size $\langle s \rangle$ [3][4].

Permalloy and Sendust are trade names of alloys having compositions leading to simultaneous near zero magnetocrystalline anisotropy K and magnetostriction constant λ_s . In this way, also the anisotropy induced by local or applied stress σ , $K_\sigma = (3/2) \lambda_s \sigma$, is minimized. Permalloy has typical composition $Fe_{15}Ni_{80}Mo_5$ and attains vanishing magnetocrystalline anisotropy by compensation of the positive K of Fe with the negative K of Ni. Sendust is the ternary alloy $Fe_{85}Si_{9.5}Al_{5.5}$, which is obtained in powder form and typically shaped as consolidated cores and magnetic heads. Because of their vanishing intrinsic anisotropy, Permalloy tapes are sensitive to magnetic field annealing and the correspondingly induced anisotropy. Consequently, they can display a range of hysteresis loop shapes, besides excellent response to broadband applications, but, like the Sendust alloy, they are somewhat niche materials. Actually, in many such applications the nanocrystalline alloys have a competitive advantage, as they come at a fraction of the cost and, as shown in Table 1, they are endowed with far higher saturation polarization, (thereby withstanding better a DC field bias), while displaying superior temperature stability and similar versatility and magnetic softness. Nanocrystalline ribbons represent a smart alternative, as they can, in spite of their metallic features, display excellent soft magnetic behavior at very high frequencies, as required, for example, in inductors of high-power-density switch-mode power supply (SMPS). Vanishing magnetocrystalline anisotropy is achieved in these alloys thanks to their nanogranular structure, obtained by homogeneous crystallization of a precursor amorphous alloy, produced by rapid solidification [5][6]. Here the anisotropy fluctuates in direction from grain to grain, on a much smaller scale than the exchange length L_{ex} , which encompasses a large number of nanometer-sized crystals. The magnetic moments in the grains are therefore constrained to alignment by the exchange interaction and cannot follow the random directions of the local easy axes. The local magnetic anisotropy K_1 is then averaged out to a residual anisotropy K_0 across the N structural units of average size δ within the volume $L_{ex}^3 = N\delta^3$ according to $K_0 \approx K_1/\sqrt{N}$. For the classical case of a Finemet alloy $Fe_{73.5}Cu_1Nb_3B_9Si_{13.5}$, having average nanograin size $\delta = 10$ nm, one finds the faint residual anisotropy $K_0 \sim 2.5$ J/m³ [7][8]. The concept of random anisotropy obviously applies to the amorphous alloys, where the ordered units are aggregates of few atoms [9]. But, once the magnetocrystalline effects are made negligible, other sources of magnetic anisotropy emerge. This is the case of the magnetostrictive Fe-based amorphous alloys (like the popular $Fe_{78}B_{13}Si_9$), where local anisotropies up to some 10³ J/m³ can arise in the as-quenched ribbons, because of the magnetoelastic coupling between frozen-in stresses and magnetization [10][11]. Such stresses cannot be fully eliminated by annealing, because the treatment temperature must be sufficiently low to avoid incipient inhomogeneous crystallization. To note that in the nanocrystalline alloys also the local magnetostrictive effects are averaged out to negligible value [8]. Co-based amorphous alloys (like $Co_{67}Fe_4B_{14.5}Si_{14.5}$, $Co_{71}Fe_4B_{15}Si_{10}$, $Co_{66}Fe_5Cr_4B_{15}Si_1$) have vanishing magnetostriction ($\lambda_s \sim 10^{-8} - 10^{-7}$) and, obviously lacking any magnetocrystalline anisotropy, they can

exhibit an extremely soft magnetic behavior, fully comparable to the one of the nanocrystalline alloys (see Table 1). The Co-based amorphous alloys display great versatility and sensitivity to magnetic annealing, besides excellent broadband response. They are not affected by the extreme brittleness of the nanocrystalline alloys, but their low saturation magnetization and the costs associated with the presence of Co limit their use to specialized applications. In these alloys, the anisotropy induced by field annealing is ascribed to atomic rearrangements of the local ordered units, whose symmetry is influenced by the direction of the magnetization [12], while directional pair ordering of the Si atoms in the Fe-Si nanocrystals is invoked for the nanocrystalline alloys [8]. High uniaxial transverse anisotropies, up to some kJ/m^3 , can be induced in amorphous and nanocrystalline ribbons by annealing under tensile stress [13][14], an effect that is thought to descend from thermally activated anelastic creep and ensuing redistribution of the atomic bonds in the amorphous phase, which are frozen-in upon cooling and stress removal [15].

Figure 1 provides an overview of the quasi static magnetic behavior of Permalloy tapes, Finemet and amorphous Co-based ribbons, and sintered Mn-Zn and Ni-Zn ring samples. An example of loop shearing in the Finemet ribbon by annealing under a saturating transverse field is provided. It is remarked how this can occur by inducing quite a low transverse anisotropy ($K_{u\perp} \sim 15 \text{ J/m}^3$), a feature conducive to excellent frequency response, in terms of high permeability, high cutoff frequency, and low losses. The high transverse anisotropy induced by stress annealing provides instead a very good alternative to cut cores used as choke coils and linear inductors [16]. Nanocrystalline samples come as thin (typically around $20 \mu\text{m}$) ribbons and their resistivity is relatively high ($\rho = 118 \times 10^{-8} \Omega\text{m}$ in Finemet). These properties are helpful in limiting the energy dissipation by the eddy currents and in broadening the useful frequency band. They are shared by the Co-based amorphous alloys (see Table 1), including the resistivity value ($\rho = 141 \cdot 10^{-8} \Omega\text{m}$ in $\text{Co}_{67}\text{Fe}_4\text{B}_{14.5}\text{Si}_{14.5}$), but for the saturation magnetization. It is then verified that similar good loss and permeability behaviors up to about 1 GHz are obtained in both alloys [17][18], because of the strict similarities of their static and dynamic response to the induced anisotropy. But properly annealed amorphous ribbons are not so brittle and allow for easier and more comprehensive magneto-optical analysis of the dw dynamics than nanocrystalline samples[17].

The very high resistivity of ferrites (typically $1 - 10 \Omega\text{m}$ in Mn-Zn and some $10^5 \Omega\text{m}$ in Ni-Zn) is equally instrumental in favouring good high-frequency behavior, which, in combination with assessed preparation methods and low costs, makes these materials still privileged for mass applications. We compare in Fig. 2 the power loss versus frequency behavior, measured up to about 1 MHz at peak polarization $J_p = 200 \text{ mT}$ in sintered Mn-Zn ferrites and field annealed tapewound ring samples of Permalloy, Co-based amorphous alloys, and Finemet nanocrystalline alloys. Overall better response of the amorphous and Finemet alloys is put in evidence. To note that Fig. 2 shows the behavior of the power loss per unit volume. By referring it to the unit mass, an increased loss figure for the ferrite sample would appear, because of its lower mass density (e.g., $\delta = 4800 \text{ kg/m}^3$ vs. $\delta = 7200 \text{ kg/m}^3$ in Finemet).

For all the applicative importance of these materials and the increasing consideration deserved by the magnetic loss behavior, as dictated by trends towards miniaturization, ensuing increase of the working frequencies, and mandatory restraint of dissipation and temperature in the inductive components, comprehensive quantitative modeling of the wideband loss phenomenology is poorly assessed in the literature. This problem resides, on the one hand, in the difficulty of managing the description of the magnetization process and its evolution from quasi-static excitation up to radiofrequencies. On the other hand, the experiments reported in the literature generally deal with limited ranges of magnetizing frequency and peak magnetization values.

In this review, we discuss first the measuring methods applied to the magnetic characterization of soft ferrites and amorphous/nanocrystalline alloys from quasi-static excitation up to the limiting frequencies, often approaching the GHz range, where the magnetic response of the material is extinguished. Significant results are then discussed, in the light of recent and less recent modeling approaches. Emphasis is placed, in particular, on the specific features of the high-frequency behavior of complex permeability and losses and on the competing mechanisms of magnetization rotation and dw motion. We discuss, in particular, how the concept of loss decomposition can be preserved and made general upon the whole wide frequency range, beyond the conventional approach to energy dissipation by eddy currents. Instrumental in the treatment of the high-frequency magnetic losses is the identification of a magnetic constitutive equation associated with the rotational processes as solution of the Landau-Lifshitz equation. This applies, in particular, when rotations play a major role in the magnetization process, which is not always the case, and the alternating induction is of relatively low amplitude, thereby giving sense to a constitutive equation described in terms of complex permeability.

2. Broadband characterization: macroscopic approach and microscopic observations.

2.1 Magnetic characterization

The spinel ferrites and the amorphous and nanocrystalline alloys can display useful soft magnetic behavior upon an extremely wide range frequencies, from DC to hundreds of MHz. Their full characterization on such a wide band is not an easy task and several experimental limitations may arise on proceeding towards the radiofrequency regimes. It is therefore expedient to extract basic information on the frequency response of the material by an impedance measurement on ring samples. By use of a four-terminal LCR digital analyzer, the inductive and resistive contributions versus frequency are obtained [19] and, once the role of the winding resistance is accounted for, the real and imaginary

initial permeability components are derived. This approach has practical value and is quite the rule in the literature [20][21], but the magnetization level in the sample is generally very low and uncontrolled and the loss figure of the material is perturbed by the ohmic dissipation. Consequently, it is ill suited to quantitative assessment and modeling of magnetization process and losses. It deals exclusively with a linear regime and sinusoidal signal, whereas a variety of regimes and induction levels are observed in applications [22]. Extensive characterization under controlled sinusoidal and non-sinusoidal induction can actually be achieved with a fluxmetric setup, an example of which is schematically shown in Fig. 3. It is a standard configuration where, with careful control and suppression of the spurious contributions by the stray parameters and taking profit of the broadband capabilities of the employed arbitrary function generator, power amplifier, and digital acquisition device, the MHz region on standard ferrite components and tapewound rings is routinely attained. In a typical arrangement, a Keysight 33220A generator, an NF DC-10 MHz HSA 4101 power amplifier, and a 500 MHz TDS 724A (or HDO 4000 LeCroy) oscilloscope are employed. The spurious phase shifts between the measured primary current i_H and secondary voltage u_2 are minimized by judicious arrangement of the windings, minimum length of leads and cables, and choice of an anti-inductive shunt resistor R_H . The specific detrimental role of this resistor in introducing by stray inductance a systematic deviation in the measurement of the energy losses at high frequencies is recognized, as discussed in detail in [23]. It has therefore been suggested that in a number of cases the direct determination of the power loss by the measurement of the rate of rise of the sample temperature T_m upon application of the AC field might be preferable [24]. In fact, the magnetic power loss per unit mass P is simply related, under adiabatic conditions, to the temperature derivative dT_m/dt through the specific heat of the material c_p

$$P = c_p \frac{dT_m}{dt} \quad , \quad [\text{W/kg}] \quad (2)$$

Equation (2) compares with the standard fluxmetric derivation of the loss per unit volume

$$P = \frac{1}{T} \int_0^T H(t) \frac{dB}{dt} dt, \quad [\text{W/m}^3] \quad (3)$$

the product of field and induction derivative integrated over the period $T = 1/f$. The adiabatic conditions can only be emulated, by restraining the loss of heat to the environment. To this end, the sample is generally kept in vacuum. By identifying a heat transmission coefficient K_h and formulating a balance equation for the generated, stored and transmitted heat rates upon switch-on of the AC field at time $t = 0$, we arrive at the equation

$$P = \frac{K_h(T_m - T_0)}{1 - \exp\left(-\frac{K_h}{c_p}t\right)} \quad , \quad [\text{W/kg}] \quad (4)$$

if T_0 is the temperature of the reservoir [25]. The coefficient K_h is easily determined by fitting the exponential decrease of the sample temperature after switch-off of the field. Wideband power loss measurements by the thermometric method have been reported for Mn-Zn ferrites in [26]. The rise of sample temperature can be remarkable, however, such as to eventually impair, depending on the J_p value, the fluxmetric loss measurement at high frequencies. For example, the power loss at 5 MHz and $J_p = 50$ mT in a typical Mn-Zn ferrite sample is of the order of 5 kW/kg, which amounts, according to (2), to a maximum rate of increase of the temperature $dT/dt \sim 7$ °C/s. Fast operations and minimum sample heating can possibly be obtained by means of a pulsed field approach [27].

The typical upper frequency limit of a few MHz, intrinsic to the fluxmetric method, does not permit one to perform, in general, a full permeability and loss analysis up to the frequencies where the magnetic response of the materials is, to any practical extent, extinguished. Under these circumstances, a natural solution for high-frequency characterization is provided by the measurement of the sample impedance using a transmission line method [28]. This is quite conveniently performed using a Vector Network Analyzer (VNA), which works both as a variable frequency signal source and as a receiver. With the arrangement shown in Fig. 4, we measure the reflection coefficient $S_{11}(f)$ of a shorted coaxial line of characteristic impedance Z_0 , where a test ring sample is centrally placed at the shorted end of the line. The coefficient $S_{11}(f)$ at the sample plane is related to the impedance $Z_{sh}(f)$ of the piece of line containing the ring by the equation

$$Z_{sh}(f) = Z_0 \frac{1 + S_{11}(f)}{1 - S_{11}(f)} \quad . \quad (5)$$

If the sample thickness h is small with respect to the quarter wavelength $\lambda/4$ of the electromagnetic field, the sample is located in a node of the electric field, dielectric effects can be ignored, and the input impedance Z_{sh} of the piece of line of length $h \ll \lambda/4$ ending into the shorted termination is given by the expression

$$Z_{sh}(f) = jZ_0 \tanh(\beta h) \approx jZ_0 \beta h \quad , \quad (6)$$

where $\beta = \omega\sqrt{LC}$ is the propagation constant of the line (the phase variation of the electromagnetic wave per unit length). Since $Z_0 = \sqrt{L/C}$, we have $Z_{sh}(f) \approx j\omega Lh$. An air-filled lossless coaxial line of radii R and r and length h (Fig. 4) is endowed with field lines concentric with the inner conductor and its impedance is, according to (6), given by the equation

$$Z_{sh} = j\omega \frac{\mu_0}{2\pi} h \cdot \ln \frac{R}{r}. \quad (7)$$

If the same piece of line is filled with a magnetic ring of thickness h , a dissipation term will appear. The material is then characterized by a complex permeability $\mu = \mu_0\mu'_r - j\mu_0\mu''_r$ and the input impedance becomes

$$Z_{sh} = j\omega \frac{\mu_0}{2\pi} \ln \frac{R}{r} \cdot h \cdot (\mu'_r - j\mu''_r), \quad (8)$$

the resistive part being associated with the magnetic loss. When the ring of radii $R_m \leq R$ and $r_m \leq r$ does not fit the line, Z_{sh} is obtained as the sum of the impedance provided by the region occupied by the material, given by (8) with R_m and r_m in place of R and r , and the impedance of the remaining air-filled part. It is essential in this case that the sample be centered in the coaxial line, that is, concentric with the field lines, in order to avoid demagnetizing effects. Two measurements of $Z_{in,sh}$ are thus performed, with and without the sample inserted in the line. From the difference $\Delta Z = \Re\{\Delta Z_{sh}\} + j\Im\{\Delta Z_{sh}\}$ the real and imaginary components of the permeability are obtained, according to the equations

$$\mu'_r = 1 + \Im\{\Delta Z_{sh}\} / \left(\omega \frac{\mu_0}{2\pi} h \cdot \ln \frac{R_m}{r_m} \right) \quad \mu''_r = \Re\{\Delta Z_{sh}\} / \left(\omega \frac{\mu_0}{2\pi} h \cdot \ln \frac{R_m}{r_m} \right), \quad (9)$$

together with the related quantities $\tan \delta = \mu''_r / \mu'_r$ and $Q = 1 / \tan \delta$.

At very high frequencies, the condition $h \ll \lambda/4$ may not be fulfilled, because the wavelength in the material shortens to $\lambda_m \cong \lambda_0 / \sqrt{\varepsilon'_r \mu'_r}$, where $\lambda_0 = 1/f \sqrt{\varepsilon_0 \mu_0}$ is the free-space wavelength and ε'_r is the relative dielectric permittivity. Mn-Zn ferrites display an extremely high DC permittivity, typically of the order of some 10^5 and, in spite of its rapid decrease with frequency, it might happen that in very large samples λ_m becomes comparable with h at high frequencies. Consequently, dimensional resonance, in combination with eddy currents, may cause abnormal increase of the loss [29]. Let us therefore consider a typical Mn-Zn ring sample with $h = 5$ mm at 1 GHz. At this frequency, we are well beyond the ferromagnetic resonance and $\mu'_r \sim 1$. By estimating $\varepsilon'_r \sim 10$ at such frequency, we get $\lambda_m/4 \sim 25$ mm.

The measured high-frequency $\mu'(f)$ and $\mu''(f)$ behaviors can be affected to some degree by systematic uncertainty and correction for it may call for a reference sample. Alternatively, one can measure the initial permeability on a lower and partially overlapping frequency interval by the fluxmetric method, for which the measurement uncertainty is known and traceability to the appropriate standards is at hand. What we do, in practice, is to measure fluxmetrically J_p up to a few MHz at a defined very low J_p value, more or less corresponding to the value expectedly attained at such frequencies by the transmission line measurement on the same ring sample. Obviously, the VNA works at defined incident power (either 1 mW or 10 mW, using the Agilent 8753A VNA), which implies decreasing J_p with increasing frequency. We can verify, however, that the involved J_p values are generally so low (around 1 - 2 mT and lower) that $\mu'(f)$ and $\mu''(f)$ become independent of it in many instances [30]. This could be guessed from the Rayleigh law $\mu(H) = a + bH$ at such J_p values, where the irreversible contribution bH is much smaller than the reversible permeability a . It is then understood how one can correspondingly obtain the largely overlapping fluxmetric and VNA wideband $\mu'(f)$ behaviors in a Mn-Zn ferrite ring, as shown for $J_p = 2$ mT in Fig 5a. Here we note that $\mu'(f)$ falls, beyond a few hundred kHz, on the VNA measured quantity also at a polarization as high as $J_p = 50$ mT, scarcely complying with the notion of initial permeability. This kind of response is typical of the sintered Mn-Zn and Ni-Zn ferrites and of the transverse-anisotropy amorphous and nanocrystalline tapes, where the role of rotations is prominent. On approaching the MHz range, the dws become eventually stuck, at least at low inductions, by the dissipative processes and only the rotations provide for the magnetization reversal. In the limit of small oscillations and for isotropically distributed easy axes (e.g., in sintered ferrites), the rotational permeability μ_{rot} depends only slightly on J_p , at least up to $J_p/J_s \sim 0.1 - 0.2$. This justifies the observed coalescing of the $\mu'(f)$ (and $\mu''(f)$) curves in the upper frequency range and of the correspondingly calculated energy loss

$$W(f) = \pi J_p^2 \mu'' / (\mu'^2 + \mu''^2), \quad [\text{J/m}^3] \quad (10)$$

shown for an N30-type Mn-Zn ferrite in Fig. 5b. This conclusion equally applies, by virtue of a quasi-linear $J(H)$ curve (see Fig. 1), to the transverse-anisotropy nanocrystalline and amorphous ribbons, up to pretty large J_p/J_s values. This is shown for a Finemet tape in Fig. 6 and is discussed in [30][31]. It is fair to stress, in any case, that the experimental limitations of the fluxmetric approach occurring at high frequencies and medium-to-high J_p values compound with conceptual hurdles in the definition of complex permeability in strongly non-linear materials, devoiding (10) of physical meaning. This is what we expect, for example, with extra-soft nanocrystalline or amorphous alloys annealed under longitudinal field, which display rectangular DC hysteresis loops (see Fig. 1). Fig. 7 shows, however, that the required approximation of near-elliptical loops holds, for example, for $J_p = 100$ mT ($J_p/J_s \sim 0.25$) in conventional Mn-Zn ferrites.

2.2 Domain wall dynamics by high-speed Kerr imaging

The indirect evidence, arising from the permeability and loss behaviours, of the competing roles of dw displacements and rotations and the eventual disappearance of the former at sufficiently high frequencies, both in ferrites and amorphous/nanocrystalline alloys, becomes a manifest effect in the specific instances where the domains and the dynamics of the dws can be directly observed by Kerr imaging. Amorphous/nanocrystalline strips annealed under a transverse saturating field are endowed with a more or less sharp transverse domain structure, depending on the specifically adopted thermomagnetic treatment and the ensuing value of the induced transverse anisotropy [32]. Under the action of an applied longitudinal field, both dw displacements and rotations occur and can be distinguished by dynamic Kerr measurements. The classical magneto-optical Kerr technique can in fact be extended up to very high frequencies by means of advanced stroboscopic methods [33], where, under the condition of repeatable domain structure, image acquisition can be made over an extremely short time interval upon a large number of successive cycles. High-speed time-resolved Kerr analysis on strip samples can be carried out, in combination with fluxmetric measurements, with the setup schematically shown in Fig. 8. The strip under investigation, placed between the pole faces of a double-C Mn-Zn ferrite core, is endowed with a small solenoid, exactly fitting the inner diameter of the core, and a few-turn tiny pickup coil, by which the fluxmetric measurement according to the scheme shown in Fig. 3 is made. After removing the upper portion of the double-C yoke and the solenoid, the strip is placed in the focal plane of a wide-field Kerr microscope, based on a Zeiss Axioscop 2 Plus device. The lower yoke now provides both exciting field and flux-closure. The CCD camera is coupled with a gated image intensifier, placed upon the ocular of the Kerr microscope, ensuring high time resolution, namely apertures as short as 50ps. The synchronization with respect to the trigger is controlled by a dedicated external delay unit. A circular spot of diameter 1.3 mm with pixel size of 2.9 μm is illuminated close to the pickup coil. An additional generator, slaved to the field signal generator, synchronously triggers the acquisition of equally time-spaced images along the hysteresis half-loop. The number of averaged acquisitions, ranges from 10^4 at low frequencies ($f < 1$ kHz) to 10^7 for $f > 1$ MHz. Defocusing due to thermal expansion of the sample poses an upper limit to the combination of high frequencies and high J_p values.

We show in Fig. 9a an example of instantaneous domain structure corresponding to a defined value (J, H) of the hysteresis loop in a transverse anisotropy ($K_L \sim 50$ J/m³) $\text{Co}_{71}\text{Fe}_4\text{B}_{15}\text{Si}_{10}$ ribbon magnetized at 100 kHz and peak polarization $J_p = 400$ mT. The image is the result of an average of about 10^6 frames and subsequent subtraction of the background (the fully saturated sample). By making the difference of the images taken at $+J_p$ and $-J_p$, the area swept by the walls emerges either as a black or white stripe, depending on the direction of motion of the walls. It is noted that parts of the same wall can move in opposite directions. Indeed, although the pressure by the applied field is close to zero, the walls are set in motion, because the rotation of the magnetization modifies the magnetostatic energy at the ribbon edges and the dw spacing tends to correspondingly modify. As the experiments show, no net transverse magnetization is created [17], but a dw related loss is inevitably generated. But the restraining action of the loss related counterfield on the dw motion, depending on the rate of change of the magnetization across the wall, is much higher than the one accompanying the large scale rotational processes. It turns out that, on increasing the frequency, the dw displacements are increasingly unfavoured and are subject to earlier relaxation with respect to the rotations. The differential dynamic Kerr images in Fig. 10, illustrating the case of a transverse anisotropy Co-based ribbon magnetized between $J_p = \pm 150$ mT up to 2 MHz, provide a clear example of increasingly hindered dw motion with increasing frequency. They also show how different parts of a same wall can move in opposite directions.

Eddy currents are not the sole responsible for magnetic energy dissipation. In the highly resistive sintered ferrites their role can even become negligible and spin damping, intended as a direct flow of energy by spin wave decay from the precessing spins to the lattice, is invoked. Also in this case, however, the experimental evidence points to precocious relaxation of the dw motion under increasing frequency.

3. A theoretical assessment of the broadband magnetic properties of ferrites and nanocrystalline alloys.

The investigation of the soft magnetic materials for high-frequency applications is chiefly directed at the behavior of two basic technical parameters: initial permeability and magnetic losses. They are not independent quantities and, under the condition of small signal amplitude and defined J_p value, they are in a direct relationship, as quantified by (10). The initial permeability is measured under a very weak field, typically by means of an impedance analyzer, and the J_p value is not held constant with frequency. J_p is so small, however, that the measured permeability value becomes independent of it in practice, the linear approximation holds, and (10) is fully appropriate. Under these conditions, the broadband soft magnetic response of the material is qualitatively classified through the Snoek's product $\mu_{rDC}f_0$, where μ_{rDC} is the relative DC permeability and f_0 is the cutoff frequency. In soft ferrites one usually finds that such a product is quite independent of the specific structural properties of the core. This is understood under the assumption of prominent role by rotations, where, for isotropic distribution of easy axes and $\mu_{rDC} \gg 1$, we estimate $\mu_{rDC} f_0 = \gamma J_s / 3\mu_0$, where γ is the free-electron gyromagnetic ratio [34]. However, the landscape of the working conditions of soft cores in present-day electronic applications is too wide for a simple approach based on the initial permeability, as one is expected to deal with a range of induction values and waveforms and the role of different materials, endowed with a variety of structural properties, needs often to be assessed upon several frequency decades. The materials of interest can be structurally homogeneous or heterogeneous, they can either be metals or poor conductors, and subject to different microscopic dissipation mechanisms. The question is therefore posed, in the absence of a comprehensive theoretical appraisal of their broadband behavior, on how far we can rely on and extend the models developed for the conventional steel sheets employed in the electrical machines, that is, at the typical industrial frequencies. A most successful interpretative approach, overcoming the intrinsic limitations of often-adopted empirical descriptions, like the ones based on the Steinmetz's model, is offered by the statistical theory of losses (STL), a physically grounded model developed for the prediction of the eddy current losses in steel sheets. This model provides solid foundation to the concept of loss separation [35][36] and, in combination with the Preisach model of magnetic hysteresis and its dynamic version [37], it can be applied, with the help of numerical methods, also for prediction in the presence of skin effect using a defined hysteretic constitutive equation [38]. But, on proceeding towards the MHz range and further, both with metallic tapes and the poorly-conductive/nonconductive ferrites, we should re-adjust to quite a general view of loss separation and loss components. This would account, on the one hand, for energy dissipation by spin relaxation to the lattice, and, on the other hand, for the expected high-frequency evolution of the magnetic constitutive equation.

3.1 Energy loss and permeability in sintered soft ferrites.

The intrinsic magnetic softness, the low-to-negligible electrical conductivity, the inexpensive raw materials, and the well-established mass production make the sintered low-anisotropy spinel ferrites the material of choice for inductive components in broadband applications. But the widespread use of the Mn-Zn and Ni-Zn ferrites is not associated with clear consensus and quantitative physical modeling regarding role and proportion of the different microscopic mechanisms lying behind the observed frequency response of permeability and energy losses [39][40][41]. The dw displacements and the rotations actually combine and compete in providing the magnetization reversal, and both relaxation and resonant effects have been envisaged for these processes. Certain difficulties also exist in Mn-Zn ferrites in treating the evolution of the electrical properties with frequency, because the eddy current patterns evolve under increasing f from grain-confined to homogeneously distributed across the sample cross-section [42].

It has been suggested in recent times that the Statistical Theory of Losses and the correspondingly derived physical concept of loss separation, where the measured energy loss $W(f)$ is expressed as the sum of hysteresis (quasi-static), excess, and classical components $W(f) = W_{hyst} + W_{exc}(f) + W_{cl}(f)$, can be comprehensively extended to the case where the mechanism of spin damping, alone or in combination with eddy current damping, takes place [43]. This amounts to state that these two viscous mechanisms follow strictly similar equations at a mesoscopic level (for example, at the scale of dws and domains), where the statistical distribution of the locally involved coercive fields regulates the sequence of irreversible processes under an applied field $H_a(t)$. It is well known, in fact, and proved by the experiments that a very same equation can describe the dynamics of a wall overcoming the static frictional pressure offered by the coercive field H_c in conducting and in insulating single crystals [44]

$$2J_s(H_a - H_c) = \beta \dot{x} \quad . \quad (11)$$

The damping coefficient β , proportionally relating the pressure of the dynamic field $H_{exc} = H_a - H_c$ and the wall velocity \dot{x} , is the sum of both eddy currents and spin damping coefficients $\beta = \beta_{eddy} + \beta_{sd}$. For a rigid isolated wall moving in a slab of conductivity σ and thickness d , the eddy current coefficient is $\beta_{eddy} = 4\sigma J_s^2 G d$, with the dimensionless coefficient $G = 0.1356$ [35]. If the slab material is non-conducting, like in the classical experiment by Dillon and Earl on a Mn ferrite single crystal [44], the spin damping coefficient becomes $\beta_{sd} = (2J_s / \mu_0 \gamma \delta) \cdot \alpha$, where γ is the electron gyromagnetic ratio, δ is the dw thickness, and α the Landau-Lifshitz damping constant [45]. Eq. (11)

identifies the energy dissipation occurring inside and, with eddy currents, around the moving d.w.. The coercive field H_c is related to the quasi-static energy loss and H_{exc} provides the additional frictional force hindering the wall motion as a whole under dynamic conditions. In particular, the fast microscopic jumps of the dws (the localized Barkhausen reversals) generate both microeddy currents and direct release of energy to the lattice by spin damping and the corresponding energy dissipation per unit volume is $W_{hyst} = 4H_c J_p$. In metallic samples, the localized eddy currents dominate over spin damping, while H_{exc} is related to the eddy currents circulating around the moving dws. Actually, the experiments of Dillon and Earl show that extra-dissipation proportional to the dw velocity occurs also in the insulating ferrites, and we can identify, for both conducting and non-conducting materials, the dw related excess loss $W_{exc} = 4H_{exc} J_p$. Of course, a real sample hosts a multitude of dws and a statistics is required to deal with the great complexity of their motion. As shown by Bertotti [35], such a statistics must take into account that the dws generally move in a correlated fashion and one identifies the correlation regions as “magnetic objects”. In polycrystalline materials, the grains are reasonably identified with the magnetic objects (MO).

The local eddy currents obviously diffuse and give rise, according to Maxwell’s equations, to a defined pattern across the sample cross-section under steady state. This is the pattern one would predict for an infinitely dense domain structure (or, equivalently, assuming a fictitious structureless material). The correspondingly predicted loss is the classical component, expressed for a bar-like sample of aspect ratio R and cross-sectional area S under sinusoidal flux as

$$W_{cl,eddy}(J_p, f) = \left(\frac{\pi^2}{6}\right) \sigma'(12k(R)S)J_p^2 f \quad , \quad [\text{J/m}^3] \quad (12)$$

where $k(R)$ is well described as an increasing function of R , $k(R) = 0.0744R - 0.0434R^2$, saturating at the value $k(R) = 0.035$ for $R = 1$ [46]. In the limit of infinitely extended sheet of thickness d , we obtain $12k(R)S = d^2$ and the standard formula for $W_{cl,eddy}(J_p, f)$ is retrieved. To note the use of the real part σ' of the conductivity in (12). It takes into account the fact that σ can be a complex quantity in a heterogeneous assembly of grains. This is what occurs in the sintered Mn-Zn ferrites, which are composed of semiconducting grains and insulating nanometer thick grain boundaries and electrically behave as an RC network. While eddy current effects are negligible in the highly insulating Ni-Zn ferrites, sintered Mn-Zn cores are the seat of eddy currents, which circulate inside the grains at low frequencies and progressively invest the whole cross-sectional area of the sample under increasing f [42]. Consequently, the conductivity is endowed with real and imaginary components, with σ' monotonically decreasing with f and σ'' passing through a maximum value at intermediate frequencies [47]. With such evolving eddy current distribution, Eq. (12) can be applied to the individual grains at low frequencies and to the whole sample cross-section at high frequencies, employing the grain conductivity and the overall conductivity at high frequencies, respectively.

The problem of making a full prediction versus frequency of $W_{cl,eddy}(f)$ in the Mn-Zn ferrites is thus complicated by σ being a complex quantity and by the evolution of the eddy current patterns with frequency. Such a prediction has been provided in recent times, by formulating the electromagnetic field equations making use of a variational multiscale approach, which leads to a simplified numerical solution [48]. This procedure requires, besides knowledge of the sample geometry and grain size, the full electrical characterization of the material up to about 10 MHz. It is remarkable, however, that eddy currents need a sufficiently large sample to play a role and, in most cases, this occurs only on entering the MHz range. This is illustrated by the frequency behavior of the energy loss for $J_p = 10\text{mT}$ in N87-type ring samples of different size shown in Fig. 11. Up to about 1 MHz, no difference ascribable to the sample size can be put in evidence. Above such a frequency, higher loss is exhibited by the largest ring, which is due to the eddy current classical contribution $W_{cl,eddy}(f)$, as predicted by the formulation provided in [48].

We might of course verify the possible role by the eddy current related excess loss $W_{exc,eddy}(f)$, which is generated by the motion of the dws simultaneous with the spin damping contribution $W_{exc,sd}(f)$, according to (11) and the involved damping coefficients β_{eddy} and β_{sd} . Since we deal with a granular materials and the motion of the walls and the immediately surrounding eddy currents are basically confined within the grains, we have now $\beta_{eddy} = 4\sigma J_s^2 G \langle s \rangle$, where the average grain size $\langle s \rangle$ is typically around 20 – 50 μm and the grain conductivity σ is about 10 - 20 $\Omega^{-1}\text{m}^{-1}$. On the other hand, $\beta_{sd} = (2J_s / \mu_0 \gamma \delta) \cdot \alpha$ is quite independent of the structural details and, with $\gamma = 1.76 \cdot 10^{11} \text{ T}^{-1}\text{s}^{-1}$, a domain wall thickness $\delta \sim 1 \mu\text{m}$, and $\alpha = 0.04$, we get $\beta_{sd} \sim 0.1 \text{ Jsm}^{-4}$ versus $\beta_{eddy} \sim 10^{-4} \text{ Jsm}^{-4}$. The grain conductivity is thus sufficiently low to make $W_{exc,eddy}(f)$ negligible with respect to $W_{exc,sd}(f)$. We pose then $W_{exc}(f) \equiv W_{exc,sd}(f)$ and derive it, by virtue of Eq. (11), closely following the approach of the Statistical Theory of Losses. To simplify the matter, we assume a constant magnetization rate \dot{J} at a given frequency f and we find the dynamic frictional field $H_{sd}^{(W)}$ in the hypothetical limiting case where the magnetization reversal is carried out by one single dw (i.e. MO) inside a grain. The wall velocity associated with the flux rate $\dot{\Phi} = 2J_s \langle s \rangle \dot{x} = 4J_p S f$ across the sample cross-section can then be expressed as

$$\dot{x} = 2 \frac{S}{\langle s \rangle} \cdot \frac{J_p}{J_s} \cdot f \quad (13)$$

and, according to (11), we obtain the field

$$H_{sd}^{(W)} = \beta_{sd} \frac{S}{\langle s \rangle} \cdot \frac{J_p}{J_s^2} \cdot f . \quad (14)$$

The magnetization reversal at a given frequency f will be actually shared at a given instant of time by a number n of MOs, whose speed will be then reduced in inverse proportion. The dynamic counterfield will then become $H_{exc} = H_{sd}^{(W)}/n$. The n simultaneously active MOs are bound to increase, together with H_{exc} , with the frequency. Since $H_{sd}^{(W)}$ is proportional to f , the law of increase of H_{exc} , that is of the excess loss $W_{exc} = 4H_{exc}J_p$, with f will necessarily be less than linear. According to Bertotti [36], we can quite generally assume a relationship between n and H_{exc} of the type

$$n(H_{exc}) = n_0 + \left(\frac{H_{exc}}{V_0}\right)^m \quad (m \leq 1), \quad (15)$$

where V_0 is a statistical parameter depending on the distribution of the local coercive fields and $n_0 = \lim_{f \rightarrow 0} n$. For a uniform distribution, $m = 1$. Disregarding for the time being n_0 , it turns out from (14) and (15) that the excess loss in ferrites at a given J_p value is given, for assumed full reversal by dw motion and triangular flux waveform ($j = \text{const.}$) by the equation

$$W_{exc}^{(tri)}(J_p, f) = 4J_p \left(\frac{\beta_{sd} S V_0^m J_p f}{\langle s \rangle J_s^2}\right)^{1/(1+m)} \quad (m \leq 1). \quad [\text{J/m}^3] \quad (16)$$

With $m = 1$, we retrieve the usual square root dependence of the excess loss on frequency exhibited by steel sheets at power frequencies. We actually know that, depending on J_p , a substantial portion of the magnetization reversal in ferrites is accomplished by rotations and the flux is ubiquitously sinusoidal. By considering the dw contribution $J_{p,dw} < J_p$ and sinusoidal $J(t)$, Eq. (16) changes into

$$W_{exc}^{(sin)}(J_{p,dw}, f) = \left(\frac{2\pi}{4}\right)^{\frac{1}{1+m}} \lambda(m) J_{p,dw} \left(\frac{\beta_{sd} S V_0^m J_{p,dw} f}{\langle s \rangle J_s^2}\right)^{1/(m+1)} \quad (m \leq 1), \quad [\text{J/m}^3] \quad (17)$$

where

$$\lambda(m) = \int_0^{2\pi} |\cos \alpha|^{(2+m)/(1+m)} d\alpha . \quad (18)$$

For $m = 1$, it is $\frac{W_{exc}^{(sin)}(J_{p,dw}, f)}{W_{exc}^{(tri)}(J_{p,dw}, f)} = 1.096$. As previously remarked, the dw displacements will fully relax in favour of the rotational processes at high frequencies. Consequently, W_{exc} will tend to vanish, following the decrease of $J_{p,dw}$.

The excess loss in steel sheets is experimentally obtained, as a rule, by subtracting $W_{hyst}(J_p)$ and $W_{cl,eddy}(J_p, f)$ from the measured energy loss $W(J_p, f)$. In the low anisotropy soft ferrites, however, we need to account for the role of the rotations and the mechanism of damping affecting the magnetic moments that oscillate inside the domains. The oscillation amplitude fluctuates from grain to grain, as imposed by the local value of the anisotropy field, but to incomparably smaller degree than the sharp variations imposed by the full moment transitions occurring inside the moving wall, responsible for W_{hyst} and W_{exc} . The scale of eddy currents generated by the spins rotating inside the domains is thus sufficiently large to be included in the classical loss component $W_{cl,eddy}(J_p, f)$ (Fig. 11). The problem therefore is posed of providing a formulation for the rotational loss $W_{rot,sd}(J_p, f)$ due to spin damping. To this end, we take profit of the quasi-linear behavior exhibited by the soft ferrites up to reasonable J_p values (see Fig. 7), of absolute interest for the high-frequency applications. We thus describe the viscous rotational response of the spins inside the magnetic domains to the applied AC field by the Landau-Lifshitz-Gilbert (LLG) equation and we start by considering the classical case of a domain endowed with anisotropy field H_k , normally directed with respect to the exciting field of frequency $\omega = 2\pi f$. The response of the spin assembly is given, in terms of the real and imaginary susceptibilities, as [45]

$$\chi'_{rot}(\omega, H_k, \pi/2) = \frac{\gamma^2 \mu_0^2 H_k M_s [\gamma^2 \mu_0^2 H_k^2 - (1 - \alpha^2) \omega^2]}{[\gamma^2 \mu_0^2 H_k^2 - (1 + \alpha^2) \omega^2]^2 + 4 \alpha^2 \gamma^2 \mu_0^2 H_k^2 \omega^2} \quad (19a)$$

$$\chi''_{rot}(\omega, H_k, \pi/2) = \frac{\gamma^2 \mu_0^2 H_k M_s [\gamma^2 \mu_0^2 H_k^2 + (1 + \alpha^2) \omega^2]}{[\gamma^2 \mu_0^2 H_k^2 - (1 + \alpha^2) \omega^2]^2 + 4 \alpha^2 \gamma^2 \mu_0^2 H_k^2 \omega^2} , \quad (19b)$$

with saturation magnetization M_s .

If we consider now the polycrystalline aggregate, we have to consider the relevant role of the intergrain demagnetizing fields, which can significantly interfere and combine with the magnetocrystalline anisotropy fields $H_{k,\text{eff}}$. We shall then have to deal with a distribution of effective anisotropy fields, which we describe by means of the lognormal function

$$g(H_{k,\text{eff}}) = \frac{1}{\sqrt{2\pi}\sigma H_{k,\text{eff}}} \exp\left[-\frac{(\ln(H_{k,\text{eff}})-h)}{2\sigma^2}\right], \quad (20)$$

where $h = \langle \ln(H_{k,\text{eff}}) \rangle$ and σ is the standard deviation of $\ln(H_{k,\text{eff}})$. We assume an isotropic orientation distribution function $p(\theta)$ for the easy axes in the half-space. It is $p(\theta) = \frac{dS(\theta)}{S} = \frac{2\pi R^2 \sin\theta}{2\pi R^2} = \sin\theta$, with $0 \leq \theta \leq \pi/2$. We integrate over amplitude and orientation of the effective anisotropy field, assuming $g(H_{k,\text{eff}})$ and $p(\theta)$ independent functions,

$$\langle \chi'_{\text{rot}}(f) \rangle = \int_0^\infty g(H_{k,\text{eff}}) dH_{k,\text{eff}} \int_0^{\pi/2} p(\theta) d\theta \chi'_{\text{rot}}(f, H_{k,\text{eff}}, \theta) \quad (21a)$$

$$\langle \chi''_{\text{rot}}(f) \rangle = \int_0^\infty g(H_{k,\text{eff}}) dH_{k,\text{eff}} \int_0^{\pi/2} p(\theta) d\theta \chi''_{\text{rot}}(f, H_{k,\text{eff}}, \theta) \quad (21b)$$

and after integration over the angular distribution, we obtain

$$\langle \chi'_{\text{rot}}(f) \rangle = \frac{2}{3} \int_0^\infty g(H_{k,\text{eff}}) \chi'_{\text{rot}}\left(f, H_{k,\text{eff}}, \frac{\pi}{2}\right) dH_{k,\text{eff}} \quad (22a)$$

$$\langle \chi''_{\text{rot}}(f) \rangle = \frac{2}{3} \int_0^\infty g(H_{k,\text{eff}}) \chi''_{\text{rot}}\left(f, H_{k,\text{eff}}, \frac{\pi}{2}\right) dH_{k,\text{eff}}. \quad (22b)$$

We remark that, as the grains increasingly pass through resonance under increasing frequency, they become transparent to the AC field and unable to compensate the magnetic poles appearing on the active surrounding grains, whose resonance frequency will on the average be raised. A grain merged in a medium of quasi-static susceptibility $\chi(f)$ will be endowed with an effective demagnetizing coefficient $N_{d,\text{eff}} \sim N_d / (1 + \chi(f))$, so that, with decreasing $\chi(f)$ at high frequencies (see Fig. 5), the local demagnetizing field are expected to increase by a quantity

$$\Delta H_d \propto \Delta N_{d,\text{eff}} \approx N_d \frac{1 - |\chi(f)|/\chi_{\text{DC}}}{1 + |\chi(f)|}. \quad (23)$$

Consequently, the distribution $g(H_{k,\text{eff}})$ will be broadened towards higher $H_{k,\text{eff}}$ values, following the decrease of the total susceptibility $\chi(f)$ with frequency. This effect is lumped into a frequency dependent quantity h in (20), according to

$$h(f) = \langle \ln\left(H_{k,\text{eff}}^{(\text{DC})} + C \frac{1 - |\chi(f)|/\chi_{\text{DC}}}{1 + |\chi(f)|}\right) \rangle, \quad (24)$$

with C a constant.

The experimental rotational permeability components $\mu'_{\text{rot}}(f)$ and $\mu''_{\text{rot}}(f)$, independent on J_p up to $J_p = 0.1J_s - 0.2J_s$, are extracted from the measured permeability by means of a self-consistent procedure, discussed in [49]. This is based on the idea that at low frequencies no rotational contribution to $\mu''(f)$ can occur. The relative permeabilities $\mu'_{\text{rot}}(f) = 1 + \langle \chi'_{\text{rot}}(f) \rangle$ and $\mu''_{\text{rot}}(f) = \langle \chi''_{\text{rot}}(f) \rangle$ are then calculated using the distribution (20) with defined value h , assuming a tentative anisotropy value consistent with the initial magnetization curve, and inserting it in Eqs. (22a) and (22b). In the successive step we take the so calculated $\chi'_{\text{rot}}(f)$ and $\chi''_{\text{rot}}(f)$ and introduce them in Eq. (24), and recalculate novel $\chi'_{\text{rot}}(f)$ and $\chi''_{\text{rot}}(f)$ behaviors. The dashed lines in Fig. 12 show the prediction of this rapidly converging procedure. By taking Eq. (10), now written as

$$W_{\text{rot}}(f) = \pi J_p^2 \mu''_{\text{rot}} / (\mu'^2 + \mu''^2), \quad [\text{J/m}^3] \quad (25)$$

we can eventually analyze the broadband $W(f)$ behavior in terms of dw and rotational contributions and proceed to the loss decomposition. To note that the total μ' and μ'' permeabilities appearing in this equation can be substituted by the calculated permeabilities μ'_{rot} and μ''_{rot} beyond about 1 MHz. The calculated $W_{\text{rot}}(f)$ curves are shown in Fig. 13 for $J_p = 2$ mT and $J_p = 20$ mT, compared with the experimental $W(f)$ curves of a $\text{Mn}_{0.821}\text{Zn}_{0.179}\text{Fe}_2\text{O}_4$ ring sample of cross-sectional area $S = 2.6 \text{ mm} \times 1.2 \text{ mm}$. With thickness $d = 1.2 \text{ mm}$, eddy current effects are negligible and we can proceed to the loss decomposition according to $W(f) = W_{\text{hyst}} + W_{\text{exc}}(f) + W_{\text{rot}}(f)$. The so obtained $W_{\text{exc}}(f)$ is shown to depend on frequency according to the power law $W_{\text{exc}}(f) \propto f^q$, with $q \sim 0.95$, that is, $m \sim 0.05$ in Eqs. (16)–(18). Physically, this implies, according to the STL, a narrow distribution of the local coercive fields and weak increase

with frequency of the MOs (or dws) active at a given instant of time. The polycrystalline aggregate lacks the homogenizing effect of eddy currents and the related mechanisms of dw bowing, instability, and multiplication.

3.2 Modeling magnetic losses in transverse anisotropy nanocrystalline alloys.

The excellent broadband properties of the transverse anisotropy nanocrystalline ribbons are apparent in the example of initial permeability versus frequency behavior provided in Fig. 6, concerning a tapewound ring sample of thickness 20.32 μm endowed with $K_{\perp} = 24 \text{ J/m}^3$. A high value of the Snoek's product $\mu_{rDC}f_0 = 3.4 \cdot 10^9 \text{ Hz}$ is associated with a residual $\mu'_r \sim 60$ at 100 MHz and a low value of the energy loss at all frequencies, as illustrated in Fig. 2. Similarly good response and frequency behavior can be found in the Co-based amorphous ribbons, whose main physical difference with the nanocrystalline alloys consists in the fairly lower saturation magnetization [8][18]. It is remarkable in Fig. 6 the fact that the increase of J_p by two orders of magnitude, from 2 mT to 200 mT, brings about relatively small increase of the DC permeability, in association with coalescing of the μ' versus frequency curves around 50 kHz - 100 kHz. This behavior descends from the existence of the previously described transverse domain structure, making rotations the dominant magnetization process. As shown in Sub-section 2.2, the dws perform substantial travel under an applied alternating longitudinal field \mathbf{H}_a , although nearly orthogonal to it, the reason residing in the evolution of the magnetic poles distribution at the ribbon edges. This implies that both the hysteresis and the excess loss components, exclusively due to the dw motion, will appear. As the Kerr experiments show, the dw displacements relax, depending on the ribbon thickness, to full extent on attaining some 100 kHz and only the rotations are involved in the upper frequency range. This amounts to state that the magnetization process is spatially uniform, if compared with the extreme localization of the domain walls. We are thus under a condition where a classical approach applies and, as shown in Fig. 1, a linear approximation holds and the DC permeability can play the role of constitutive equation. Given the typical resistivity and thickness values of the ribbon samples, we would then expect, according to the solution of the electromagnetic diffusion equation, that the skin effect should enter into play. In such a case, the frequency dependence of the classical loss should pass from the $W_{cl,eddy} \propto f$ to the $W_{cl,eddy} \propto f^{1/2}$ dependence [35]. This is never observed [17]. The point here is that the DC permeability is hardly acceptable as constitutive equation at high frequencies [50]. On the other hand, to find a dynamic constitutive equation is not an easy task. In the present case, however, we have to face the rotational process at high frequencies, under favorable geometrical conditions, where the AC field is orthogonal to the easy axis and a simple antiparallel domain structure exists. This permits us to focus on such a process and analytically solve the linearized Landau-Lifshitz equation

$$\frac{\partial \mathbf{M}}{\partial t} = -\mu_0 \gamma \mathbf{M} \times \mathbf{H}_{\text{eff}} + \mathbf{M} \times \frac{\alpha}{M_s} \frac{\partial \mathbf{M}}{\partial t} \quad (26)$$

where the dynamic parts of field \mathbf{h} and magnetization \mathbf{m} are treated as perturbations. We pose then $\mathbf{H}_{\text{eff}} = \mathbf{H}_k + \mathbf{h}$ and $\mathbf{M} = \mathbf{M}_s + \mathbf{m}$, where both \mathbf{H}_k and \mathbf{M}_s lie along the transverse x direction. The system is treated as a single domain, lumping the role of the actual antiparallel domain structure into a demagnetizing coefficient for the z direction, normal to the ribbon plane, $N_{dz} < 1$ and a demagnetizing field $h_{\text{dem}} = -N_{dz}m_z$. \mathbf{m} is composed of longitudinal m_y and vertical m_z components. Finally, the longitudinal effective field $h_{\text{eff},y}$ is the sum of the applied AC field h_a and the eddy-current counterfield h_{eddy} .

A solution of Eq. (6) can then be found by analytic method, within the harmonic approximation and an expression for the intrinsic susceptibility $\chi_{\text{int}}(f)$, playing the role of a frequency-dependent constitutive magnetic equation of the material, is derived, as demonstrated in detail in [31]. Such a quantity is then entered the Maxwell's diffusion equation, written as

$$\frac{\partial^2 h_y}{\partial z^2} = j\omega\sigma b_y, \quad (27)$$

where b_y is the AC induction. This is solved, with the appropriate boundary conditions, in conjunction with the constitutive equation

$$b_y = \mu_0(1 + \chi_{\text{int}}(f))h_{\text{eff},y} = \mu_{\text{int}}h_{\text{eff},y} \quad (28)$$

As shown in [31], the calculations eventually lead to the following expression for the energy loss, of classical character, associated with the magnetization rotations

$$W_{\text{rot}}(f) = \frac{\pi B_p^2}{2|\mu_{\text{int}}|} \cdot \frac{(\lambda' - \lambda'') \sinh(\lambda' - \lambda'') - (\lambda' + \lambda'') \sin(\lambda' + \lambda'')}{\cosh(\lambda' - \lambda'') - \cos(\lambda' + \lambda'')} \quad (29)$$

where λ' and λ'' are the real and imaginary parts of the complex quantity

$$\lambda = \lambda' + j\lambda'' = \sqrt{\frac{\omega\sigma|\mu_{\text{int}}|d^2}{2}} \cdot \left(\sqrt{\frac{1+\mu'_{\text{int}}/|\mu_{\text{int}}|}{2}} - j\sqrt{\frac{1-\mu'_{\text{int}}/|\mu_{\text{int}}|}{2}} \right). \quad (30)$$

We show in Fig. 14 an example of DC-1 GHz energy loss behavior measured on a 20.1 μm thick tapewound nanocrystalline ring sample endowed with transverse anisotropy $K_{\perp} = 15 \text{ J/m}^3$ and its decomposition into the hysteresis W_{hyst} , rotational $W_{\text{rot}}(f)$, and $W_{\text{exc}}(f)$ components. It is observed how $W_{\text{rot}}(f)$ (dashed line), calculated assuming the exchange stiffness constant value $A = 3 \cdot 10^{-11} \text{ J/m}$ and the Landau-Lifshitz damping constant $\alpha = 0.06$, fully covers the experimental $W(f)$ above a few hundred kHz. It is remarked that eddy currents appear to provide the largest contribution to $W_{\text{rot}}(f)$, with additional dissipation by spin damping recognized with f larger than about 100 MHz. The excess loss follows a power law dependence on frequency $W_{\text{exc}}(f) \propto f^q$, with the exponent $q < 1$ and decreasing with increasing J_p , and drops beyond some 100 kHz, as expected from the predicted and magneto-optically observed relaxation of the dw processes on approaching and overcoming such a frequency. The decrease of q with J_p is understood with a correspondingly increased probability for dw multiplication, in analogy with the typical response of the longitudinal dw systems.

3. Conclusions

Soft ferrites and nanocrystalline alloys owe their remarkable soft magnetic properties to intrinsically low anisotropy energy, prone to manipulation through either calibrated chemistry, like in the Mn-Zn compounds, or magnetothermal treatments in the nanocrystalline ribbons, by which strength of the anisotropy constant and direction of the easy axis can be regulated. The insulating/semi-insulating properties of the ferrites and the very low thickness of the nanocrystalline ribbons are conducive to their excellent broadband permeability and energy loss behavior, fully extending in the MHz range. In spite of widespread studies and ubiquitous applications, the theoretical/phenomenological assessment of such behavior has been hardly attained so far in the literature.

In this paper, we review, after a brief introduction regarding the general physical and magnetic properties of these materials, the main experimental techniques adopted for their characterization upon a range of frequencies extending from DC to hundreds of MHz. Attention is devoted to the traditional fluxmetric measuring method, employed up to a few MHz, and the transmission-line method using the Vector Network Analyzer, by which the GHz range can be attained. Supporting evidence to the envisaged magnetization mechanisms is provided by dynamic magneto-optical observations of the domain structure, performed by means of a high-speed Kerr setup. A useful combination of low anisotropy properties and early relaxation of the dw processes permits one to achieve frequency continuity and overlapping results on passing from one method to the other within the peak polarization intervals of interest for the high-frequency applications.

The analysis of the broadband loss and permeability properties is based, on the one hand on the appraisal of the distinct roles of dw displacements and magnetization rotations and, on the other hand, on a generalized view of concepts and formulation of the loss separation, as provided by the Statistical Theory of Losses, where spin damping and eddy currents are identified as concurring dissipation mechanisms. In such a context, the Landau-Lifshitz equation is adopted for the determination of the high-frequency magnetic constitutive equation of the material. One important outcome of this approach is that no evidence exists, both in Mn-Zn ferrites and nanocrystalline ribbons, for an established skin effect.

References

1. E.C. Snelling: Soft ferrites: properties and applications, 2nd ed. (Butterworth-Heinemann, 1989).
2. H. Pascard: Basic concepts for high permeability in soft ferrites, *J. Phys. IV France*, 8(Pr2), 377 (1998).
3. M. Rossignol: Irreversibilit  des processus d'aimantation et hyst eresis dans les mat riaux ferromagn tiques r els : le r le des d fauts, in *Magn tisme*, vol. I, edited by E. du Tr molet de Lacheisserie, Presses Universitaires de Grenoble, 1999, p. 211.
4. F. Fiorillo, C. Appino, and M. Pasquale: Hysteresis in magnetic materials, in *The Science of Hysteresis*, edited by G. Bertotti and I. Mayergoyz, Academic Press, Vol. III, 2006, p. 1.
5. Y. Yoshizawa S. Oguma, and K. Yamauchi: New Fe-based magnetic alloy composed of ultrafine grain structure, *J. Appl. Phys.* 64, 6044 (1988).
6. A. Makino, A. Inoue, and T. Masumoto: Nanocrystalline soft magnetic Fe-M-B (M=Zr, Hf, Nb) alloys produced by crystallization of amorphous phase, *Mater. Trans. JIM* 36, 924 (1995).
7. G. Herzer, Grain size dependence of coercivity and permeability in nanocrystalline ferromagnets, *IEEE Trans. Magn.* 26: 1397-1402, 1990.

8. G. Herzer: Nanocrystalline soft magnetic alloys, in Handbook of Magnetic Materials, edited by K.H.J. Buschow, Amsterdam, Elsevier, Vol. 10, 1997, p. 415.
9. R. Alben, J.J. Becker, and M.C. Chi: Random anisotropy in amorphous magnets, *J. Appl. Phys.* 49, 1653 (1978).
10. H. Kronmüller and W. Fernengel: The role of internal stresses in amorphous ferromagnetic alloys, *Phys. Stat. Sol. (a)* 64, 493 (1981).
11. C. Appino and F. Fiorillo: A model for the reversible magnetization in amorphous alloys, *J. Appl. Phys.*, 76, 5371 (1994).
12. H. Morita, Y. Obi, and H. Fujimori: Magnetic anisotropy of (Fe, Co, Ni)₇₈Si₁₀B₁₂ alloy system, in *Rapidly Quenched Metals*, edited by S. Steeb and R. Warlimont, North-Holland, Amsterdam, 1985, p. 1283.
13. L. Kraus, K. Závěta, O. Heczko, P. Duhaj, G. Vlasák, and J. Schneider: Magnetic anisotropy in as-quenched and stress-annealed amorphous and nanocrystalline Fe_{73.5}Cu₁Nb₃Si_{13.5}B₉ alloys, *J. Magn. Magn. Mater.* 112, 275 (1992).
14. F. Alves and R. Barrué: Anisotropy and domain patterns of flash stress-annealed soft amorphous and nanocrystalline alloys, *J. Mater. Eng.* 254-255, 155 (2003).
15. Y. Suzuki, J. Haimovich, and T. Egami: Bond-orientational anisotropy in metallic glasses observed by x-ray diffraction, *Phys. Rev. B* 35, 2162 (1987).
16. H. Fukunaga, N. Furukawa, H. Tanaka, and M. Nakano: Nanostructured soft magnetic material with low loss and low permeability, *J. Appl. Phys.* 87, 7103 (2000).
17. A. Magni, O. Bottauscio, C. Beatrice, A. Caprile, E. Ferrara, and F. Fiorillo: Magnetization process in thin laminations up to 1 GHz, *IEEE Trans. Magn.* 48, 1363 (2012).
18. F. Fiorillo, G. Bertotti, C. Appino, and M. Pasquale: Soft Magnetic Materials, in Wiley Encyclopedia of Electrical and Electronics Engineering, edited by Mihai Peterca, Wiley, 2016, p. 1.
19. L. Callegaro: Electrical Impedance: Principles, Measurement, and Applications (CRC Press, Boca Raton, FA, USA, 2013).
20. I. Betancourt: Magnetization Dynamics of Amorphous Ribbons and Wires Studied by Inductance Spectroscopy, *Materials* 4 37 (2011). doi:10.3390/ma4010037.
21. J. Füzer, S. Dobák, and P. Kollár: Magnetization dynamics of FeCuNbSiB soft magnetic ribbons and derived powder cores, *J. Alloys Compounds* 628, 335 (2015). doi: 10.1016/j.jallcom.2014.12.126.
22. J. Petzold: Applications of nanocrystalline soft magnetic materials for modern electronic devices, *Scr. Mater.* 48, 895 (2003). doi: 10.1016/S1359-6462(02)00624-3
23. V. Loyau, M. Lo Bue, and F. Mazaleyrat: Measurement of magnetic losses by thermal method applied to power ferrites at high level of induction and frequency, *Rev. Sci. Instr.* 80, 024703 (2009). doi: 10.1063/1.3079382.
24. B. Ahmadi, F. Mazaleyrat, G. Chaplier, V. Loyau, and M. LoBue: Enhancement of medium frequency hysteresis loop measurements over a wide temperature range, *IEEE Trans. Magn.* 52, 6100404 (2016). doi: 10.1109/TMAG.2016.2535860.
25. F. Fiorillo: Measurement and Characterization of Magnetic Materials (Elsevier-Academic Press, San Diego, CA, USA, 2004), p. 388.
26. M. LoBue, F. Mazaleyrat, and V. Loyau: Study of magnetic losses in Mn-Zn ferrites under biased and asymmetric excitation waveforms, *IEEE Trans. Magn.* 46, 451 (2010).
27. B. Tellini, R. Giannetti, G. Robles, and S. Lizón-Martínez: New method to characterize magnetic hysteresis in soft ferrites up to high frequencies, *IEEE Trans. Instr. Meas.* 55, 311 (2006).
28. R.B. Goldfarb and H.E. Bussey: Method for measuring complex permeability at radio frequencies," *Rev. Sci. Instr.* 58, 624 (1987).
29. G.R. Skutt and F. C. Lee: Characterization of dimensional effects in ferrite-core magnetic devices, *PESC '96*, vol. 2, 1435 (1996). doi:10.1109/PESC.1996.548770.
30. A. Magni, F. Fiorillo, E. Ferrara, A. Caprile, O. Bottauscio, and C. Beatrice: Domain wall processes, rotations, and high-frequency losses in thin laminations, *IEEE Trans. Magn.* 48, 3796 (2012). doi: 10.1109/TMAG.2012.2196985.
31. C. Beatrice, S. Dobák, E. Ferrara, F. Fiorillo, C. Ragusa, Ján Füzer, and P. Kollár: Broadband magnetic losses of nanocrystalline ribbons and powder cores", *J. Magn. Magn. Mater.* 420, 317 (2016). doi: 10.1016/j.jmmm.2016.07.045.
32. S. Flohrer, R. Schäfer, J. McCord, S. Roth, L. Schultz, F. Fiorillo, W. Günther, and G. Herzer: Dynamic magnetization process in nanocrystalline tape wound cores with transverse induced anisotropy, *Acta Mater.* 54, 4693 (2006). doi:10.1016/j.actamat.2006.04.040
33. D. Chumakov, J. McCord, R. Schäfer, L. Schultz, H. Vinzelberg, R. Kaltofen, and I. Mönch: Nanosecond time-scale switching of permalloy thin film elements studied by wide-field time-resolved Kerr microscopy, *Phys. Rev. B* 71, 014410 (2005). doi:10.1103/PhysRevB.71.014410.
34. D. Stoppels: Developments in soft magnetic power ferrites, *J. Magn. Magn. Mater.* 160, 323 (1996). doi: 10.1016/0304-8853(96)00216-8
35. G. Bertotti: Hysteresis in Magnetism (Academic Press, San Diego, CA, USA, 1998).

36. G. Bertotti: General properties of power losses in soft ferromagnetic materials, *IEEE Trans. Magn.* 24, 621 (1988). doi: 10.1109/20.43994.
37. G. Bertotti: Generalized Preisach model for the description of hysteresis and eddy current effects in metallic ferromagnetic materials, *J. Appl. Phys.* 69, 4608 (1991). doi: 10.1063/1.348325.
38. G. Bertotti, O. Bottauscio, M. Chiampi, F. Fiorillo, M. Pasquale, and M. Repetto: Power losses in magnetic laminations with hysteresis: finite element modelling and experimental validation, *J. Appl. Phys.* 81, 5606 (1997). doi: 10.1063/1.364614.
39. H. Saotome and Y. Sakaki: Iron loss analysis of Mn-Zn ferrite cores, *IEEE Trans. Magn.* 33, 728 (1997). doi: 10.1109/20.560105.
40. T. Tsutaoka, T. Kasagi, K. Hakateyama, and M.Y. Koledintseva: Analysis of the permeability spectra of spinel ferrite composites using mixing rules, *IEEE Proc. Int. Symp. EMC* (Denver, CO, 2013), p. 545.
41. W. A. Roshen: High-frequency tunneling magnetic loss in soft ferrites, *IEEE Trans. Magn.* 43, 968 (2007). doi: 10.1109/TMAG.2006.882750
42. M. Drogenik, A. Znidarsic, and I. Zajc: Highly resistive grain boundaries in doped MnZn ferrites for high frequency power supplies, *J. Appl. Phys.* 82, 333 (1997). doi: 10.1063/1.365817.
43. F. Fiorillo, C. Beatrice, O. Bottauscio, A. Manzin, and M. Chiampi: Approach to magnetic losses and their frequency dependence in Mn-Zn ferrites, *Appl. Phys. Lett.* 89, 122513 (2006). doi: 10.1063/1.2356111
44. J.F. Dillon, Jr. and H.E. Earl, Jr.: Domain wall motion and ferromagnetic resonance in a manganese ferrite, *J. Appl. Phys.* 30, 202 (1959). doi: 10.1063/1.1735134.
45. J.C. Peuzin: Les matériaux doux pour l'électronique haute fréquence, in *Magnétisme*, vol. II, edited by E. du Trémolet de Lacheisserie, Presses Universitaires de Grenoble, 1999, p. 155.
46. O. de la Barrière, C. Appino, F. Fiorillo, C. Ragusa, M. Lecrivain, L. Rocchino, H. Ben Ahmed, M. Gabsi, F. Mazaleyrat, and M. Lo Bue: Characterization and prediction of magnetic losses in Soft Magnetic Composites under distorted induction waveforms, *IEEE Trans. Magn.* 49, 1318 (2013). doi: 10.1109/TMAG.2012.2218614.
47. V. Loyau, G.Y. Wang, M. LoBue, and F. Mazaleyrat: An analysis of Mn-Zn ferrite microstructure by impedance spectroscopy, scanning transmission electron microscopy and energy dispersion spectrometry characterizations, *J. Appl. Phys.* 111, 053928 (2012). doi: 10.1063/1.3693544.
48. F. Fiorillo, C. Beatrice, O. Bottauscio, E. Carmi: Eddy current losses in Mn-Zn ferrites, *IEEE Trans. Magn.* 50, 6300109 (2014). doi: 10.1109/TMAG.2013.2279878.
49. C. Beatrice, V. Tsakaloudi, S. Dobák, V. Zaspalis, and F. Fiorillo: Magnetic losses versus sintering process in Mn-Zn Ferrites, *J. Magn. Magn. Mater.* 429, 129 (2017). doi: 10.1016/j.jmmm.2016.12.121
50. K. Seemann, H. Leiste, and V. Bekker: New theoretical approach to the RF-dynamics of soft magnetic FeTaN films for CMOS components *J. Magn. Magn. Mater.*, 278, 200 (2004). doi: 10.1016/j.jmmm.2003.11.402.

Table 1 – Typical compositions and basic magnetic parameters of soft magnetic materials for broadband applications.

	Composition (wt% <i>cryst. alloys</i> , at% <i>amorphous alloys</i>)	Max. relative permeability μ_{\max}	Coercive field H_c (A/m)	Saturation polarization J_s (T)	Curie temperature T_c (°C)	Saturation magnetostriction $\lambda_s = (\Delta l/l)_{J_s}$
<i>Sintered ferrites</i>	(Mn,Zn)O·Fe ₂ O ₃ (Ni,Zn)O·Fe ₂ O ₃	10 ³ -10 ⁴ 10 ² -10 ³	5 - 20 20 -200	0.4 - 0.5 0.2 – 0.35	130 – 280 110 - 400	-2·10 ⁻⁶ -20·10 ⁻⁶
Permalloy	Fe ₁₅ Ni ₈₀ Mo ₅	5·10 ⁵	0.3 -2	0.75-0.80	420	1·10 ⁻⁶
<i>Sendust</i>	Fe ₈₅ Si _{9.5} Al _{5.5}	5·10 ⁴	5-10	1.70	670	1·10 ⁻⁶
<i>Amorphous alloys (Co-based)</i>	Co ₆₇ Fe ₄ B _{14.5} Si _{14.5}	5·10 ⁵	0.5-1	0.63	320	5·10 ⁻⁷
<i>Nanocrystalline alloys (FINEMET)</i>	Fe _{73.5} Cu ₁ Nb ₃ Si _{13.5} B ₉	5·10 ⁵	0.5-1	1.24	600	2·10 ⁻⁶
<i>Nanocrystalline alloys (NANOPERM)</i>	Fe ₈₆ Cu ₁ Zr ₇ B ₆	5·10 ⁴	3	1.52	600	1·10 ⁻⁷

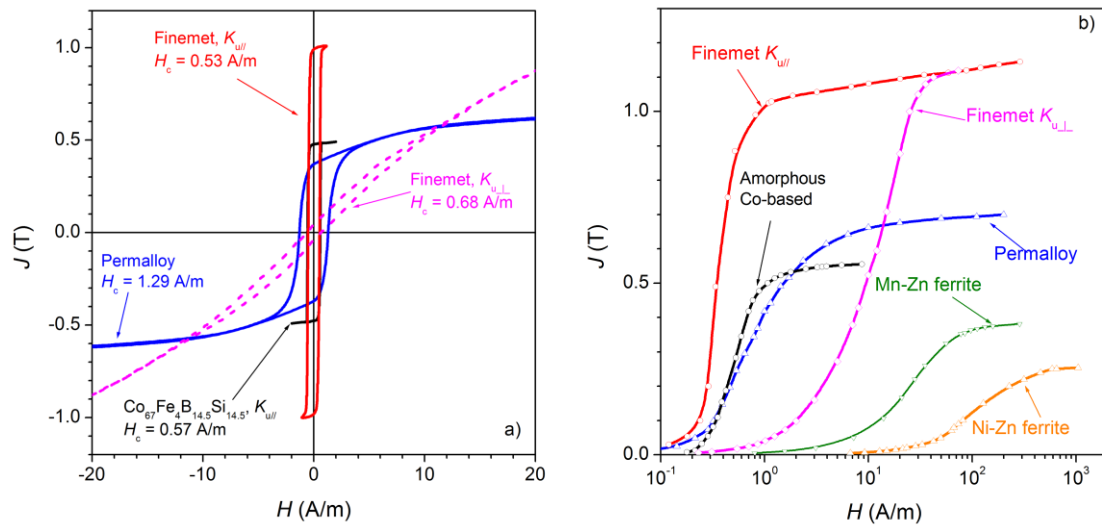


Figure 1 a) Quasi static major hysteresis loops of soft magnetic materials for broadband applications (Permalloy $\text{Fe}_{15}\text{Ni}_{80}\text{Mo}_5$, amorphous alloy $\text{Co}_{67}\text{Fe}_4\text{B}_{14.5}\text{Si}_{14.5}$, nanocrystalline (Finemet) alloy $\text{Fe}_{73.5}\text{Cu}_1\text{Nb}_3\text{B}_9\text{Si}_{13.5}$). All these materials are obtained as ribbons. Either longitudinal $K_{u//}$ or transverse $K_{u\perp}$ anisotropy are induced by annealing under a saturating magnetic field. Quasi-linear $J(H)$ curve with $K_{u\perp} \sim 15 \text{ J/m}^3$ is shown for the Finemet alloy. b) The normal magnetization curves of the same alloys are compared with those of the sintered Mn-Zn and Ni-Zn ferrites.

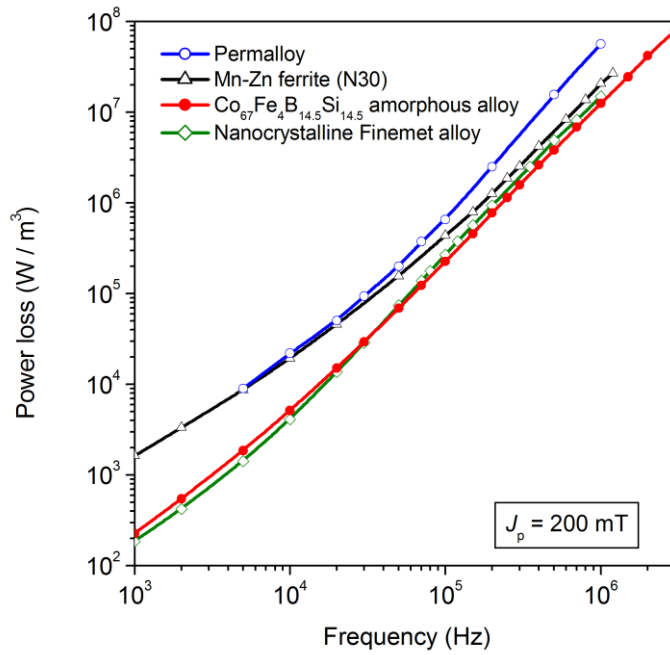


Figure 2 Power loss at intermediate and high frequencies and peak polarization value $J_p = 200$ mT in tapewound ring samples of $\text{Fe}_{15}\text{Ni}_{80}\text{Mo}_5$ Permalloy (ribbon thickness $d = 25$ μm), amorphous $\text{Co}_{67}\text{Fe}_4\text{B}_{14.5}\text{Si}_{14.5}$ alloy ($d = 13.7$ μm), nanocrystalline (Finemet) $\text{Fe}_{73.5}\text{Cu}_1\text{Nb}_3\text{B}_9\text{Si}_{13.5}$ alloy ($d = 20.3$ μm), and in a sintered Mn-Zn ferrite. The tapewound samples have been annealed under a transverse saturating field.

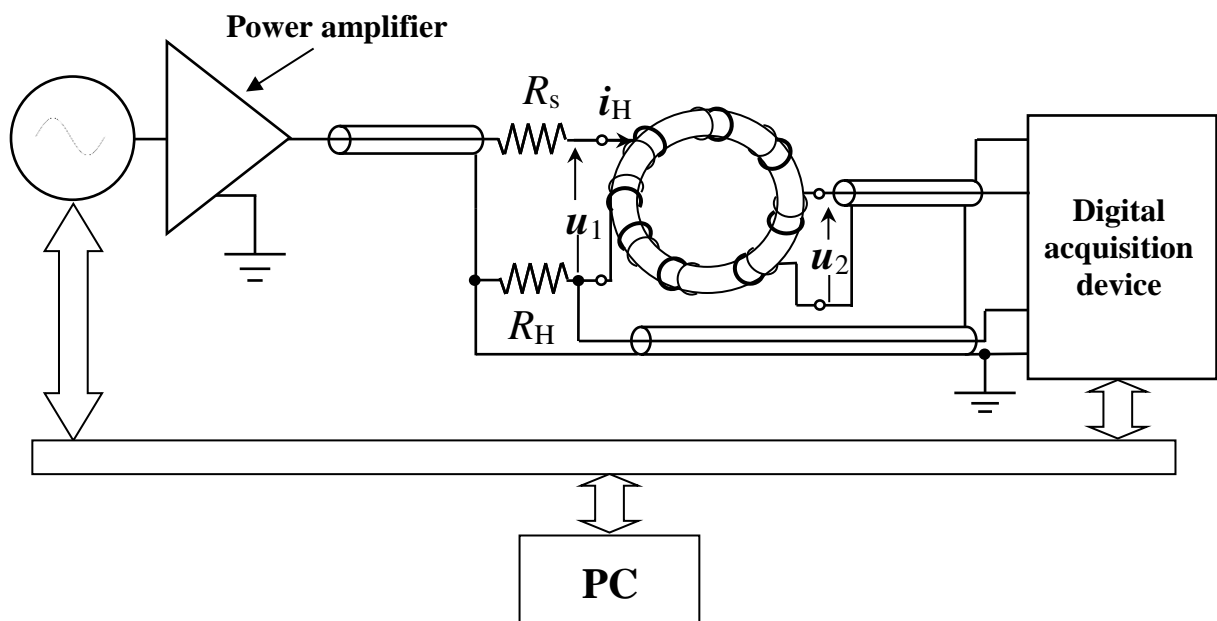


Figure 3 Scheme of a fluxmetric setup employed in the broadband measurement of hysteresis loop and losses in soft magnetic materials. The voltage drop $u_H = R_H i_H$ on the anti-inductive resistance R_H , proportional to the applied field, and the secondary voltage u_2 are fed into a high-sampling-rate acquisition device. The prescribed induction waveform is controlled by digital feedback. Number of turns and layout of the primary and secondary windings can evolve with frequency, in order to guarantee sufficiently high u_2 value at low frequencies and minimum role by the stray parameters at high frequencies.

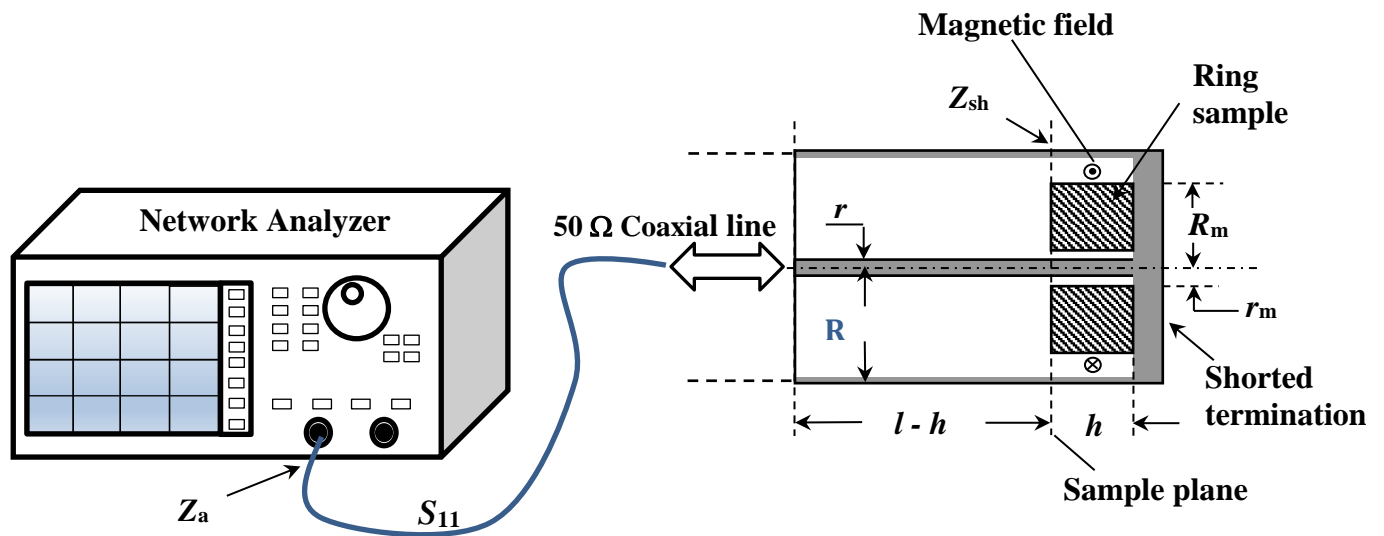


Figure 4 The complex magnetic permeability of a ring sample is obtained up to a few GHz by a transmission line method, making use of a Vector Network Analyzer (VNA) feeding a shorted 50 Ω coaxial cable, which holds the sample at its bottom. The VNA generates a frequency-swept signal and provides the frequency dependence of the complex reflection coefficient $S_{11}(f)$. This is, in turn, related to the impedance $Z_{sh}(f)$ at the sample plane by the equation $Z_{sh}(f) = Z_0(1 + S_{11}(f))/(1 - S_{11}(f))$, where Z_0 is the characteristic impedance of the line. $S_{11}(f)$ is measured at the sample plane by moving the port plane via internal software, compensating for the electrical length of the coaxial cable.

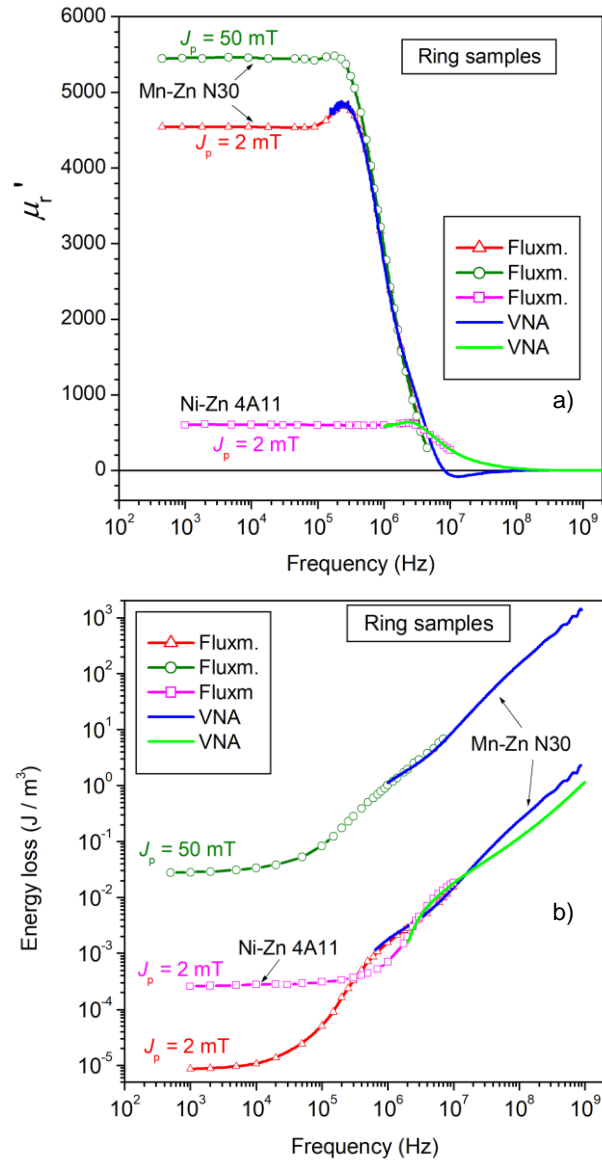


Figure 5 a) Examples of wideband behavior of the relative real permeability $\mu_r'(f)$ in Mn-Zn and Ni-Zn ferrite ring samples (outside diameter 15 mm, thickness 5.36 mm) at different J_p values. The fluxmetric and VNA results overlap in the common frequency interval. b) Corresponding behavior of the energy losses. The overlapping region shrinks on increasing J_p , because of a correspondingly increasing proportion of the domain wall processes with respect to the rotations.

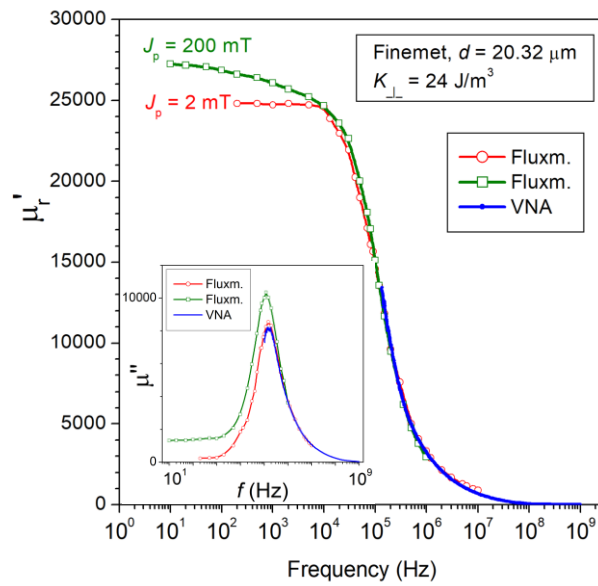


Figure 6 Real μ' and imaginary μ'' permeability components versus frequency measured at $J_p = 2 \text{ mT}$ and $J_p = 200 \text{ mT}$ in a $20.32 \mu\text{m}$ thick transverse anisotropy ($K_{\perp} = 24 \text{ J/m}^3$) nanocrystalline ribbon. Fluxmetric and VNA measurements overlap at high frequencies.

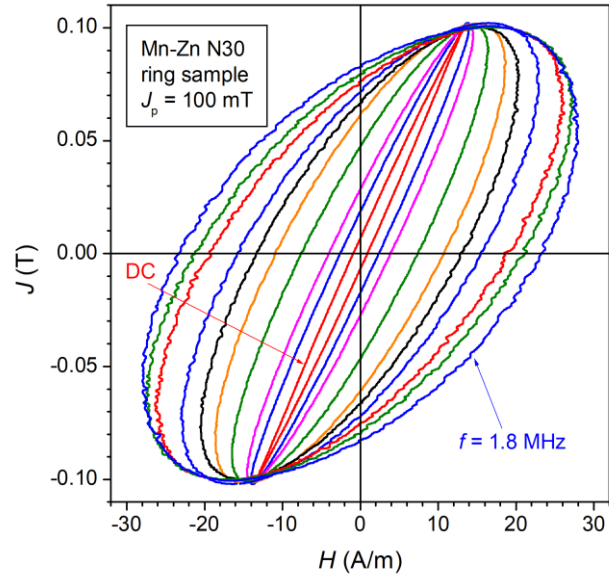


Figure 7 Evolution of the hysteresis loops under increasing magnetizing frequency at $J_p = 100$ mT in a N30 Mn-Zn ferrite. The near-elliptical shape of the loops makes realistic their description via the complex permeability.

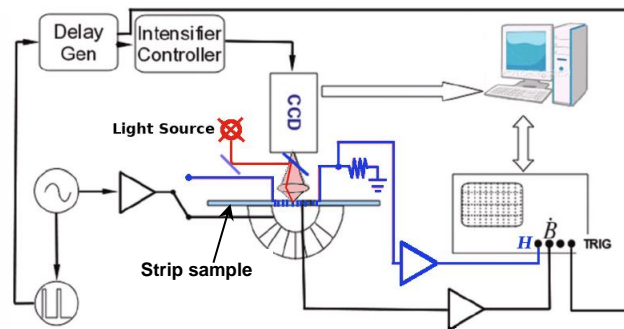


Figure 8 A magneto-optical setup for broadband time-resolved observation of the domain structure in amorphous/nanocrystalline strip samples. The core of the setup is an Intensified CCD camera, with aperture down to 50ps, synchronized via an external dedicated delay unit. The specimen, endowed with primary and secondary windings, is placed between the pole faces of Mn-Zn ferrite double-C core for the fluxmetric measurements. After removing the upper portion of the yoke, Kerr measurements are performed (switch in the lower position), with the yoke providing the exciting AC field.

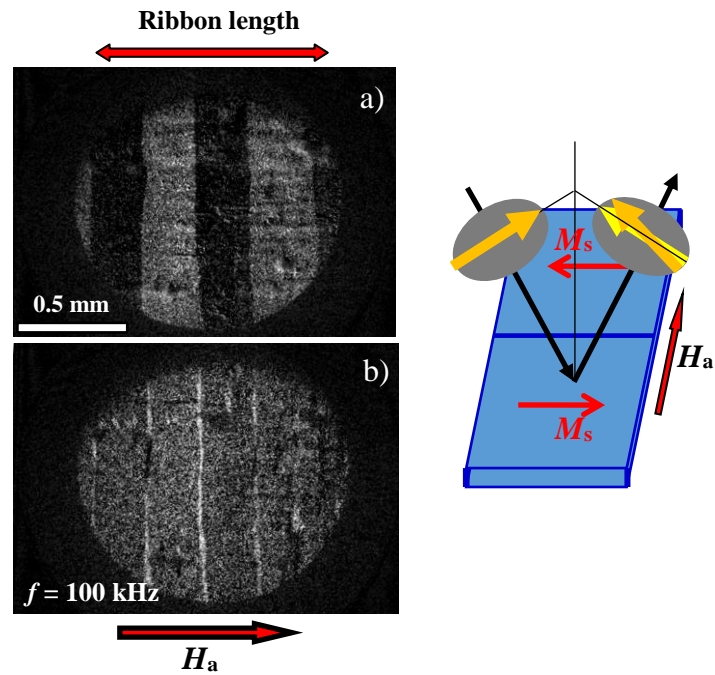


Figure 9 Dynamic domain structure observed by high-speed Kerr imaging in a transverse anisotropy ($K_{\perp} \sim 50 \text{ J/m}^3$) 19 μm thick $\text{Co}_{71}\text{Fe}_4\text{B}_{15}\text{Si}_{10}$ amorphous ribbon. a) The stroboscopic acquisition is made at a given (H , J) point of the hysteresis loop (peak polarization $J_p = 400 \text{ mT}$) at $f = 100 \text{ kHz}$. b) The white stripes emerge from the differential magneto-optical frames taken at the opposite tip points of the loop and denote the area swept by the walls upon cycling between $\pm J_p$. The gray areas are exclusively occupied by the rotational processes.

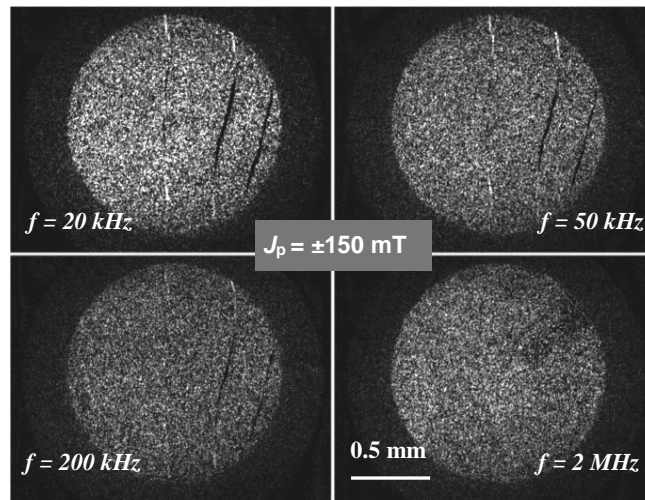


Figure 10 The dynamic images of the domain structure, taken at $J_p = \pm 150 \text{ mT}$ in a transverse anisotropy Co-based amorphous ribbon, are subtracted one to another, to reveal the displacements of the domain walls across the hysteresis loop. The area swept by the walls, exposed by the thin transverse stripes traversing the gray noise background, fully vanish at 2 MHz.

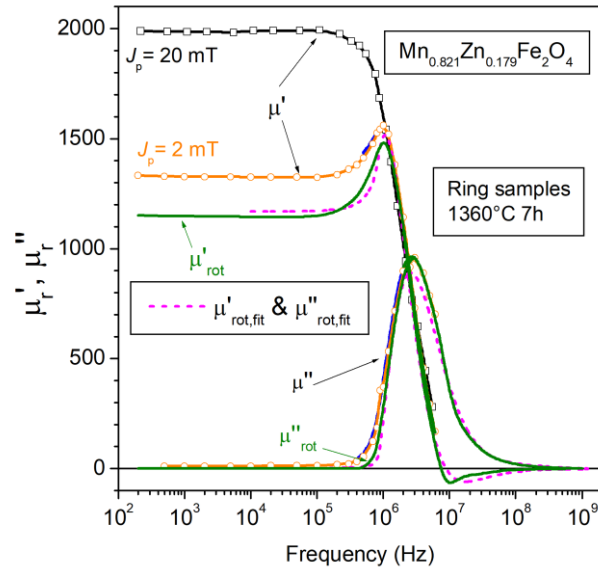


Figure 11 Real and imaginary permeability measured up to 1 GHz by combination of fluxmetric (symbols) and VNA (solid lines) methods in a Mn-Zn ring sample sintered 7 hours at 1360 °C. The rotational contributions $\mu'_{rot}(f)$ and $\mu''_{rot}(f)$ are singled out from the measured permeabilities $\mu'(f)$ and $\mu''(f)$ by a self-consistent procedure, discussed in [55]. The dashed lines show the prediction of the $\mu'_{rot}(f)$ and $\mu''_{rot}(f)$ behaviors by Eq. (15) using the Landau-Lifshitz damping parameter $\alpha = 0.04$.

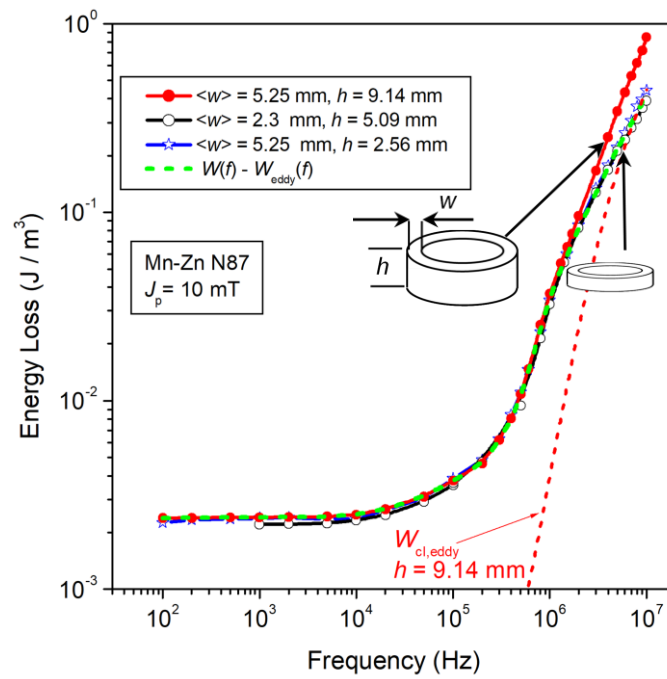


Figure 12 Magnetic energy loss $W(f)$ up to 10 MHz at $J_p = 10 \text{ mT}$ in commercial Mn-Zn ferrite rings of different size. Eddy current losses provide a measurable contribution to $W(f)$ in the largest sample only (thickness 9.14 mm), beyond about 1 MHz, as predicted by the calculated classical loss $W_{\text{cl,eddy}}(f)$ (short-dash line) [54]. By subtracting $W_{\text{cl,eddy}}(f)$ from $W(f)$, we obtain the eddy current free loss curve (dashed-line), which coincides with the curves measured on the smaller 5.09 mm and 2.56 mm thick rings.

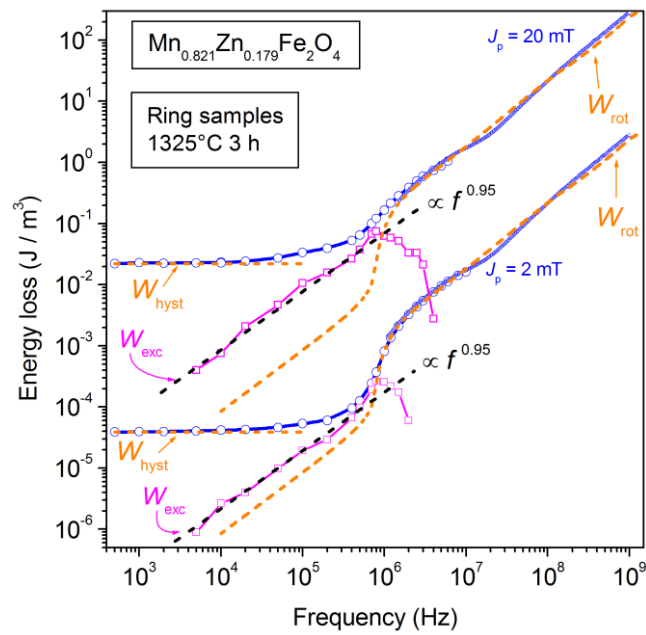


Figure 13 DC-1GHz energy loss $W(f)$ measured at two J_p levels in a Mn-Zn ring sample sintered 3 hours at 1325 °C and its decomposition $W(f) = W_{\text{hyst}} + W_{\text{exc}}(f) + W_{\text{rot}}(f)$. The 1.2 mm thick sample is free of eddy current losses. W_{hyst} is an experimental quantity, $W_{\text{rot}}(f)$ is calculated by Eq. (16), and $W_{\text{exc}}(f)$ is obtained as a difference. $W_{\text{exc}}(f)$ significantly contributes to $W(f)$ from some 50 kHz up to about 1 MHz, where it starts to drop (together with W_{hyst}). In this frequency interval it follows a law of the type $W_{\text{exc}}(f) \propto f^p$, with $p \sim 0.95$.

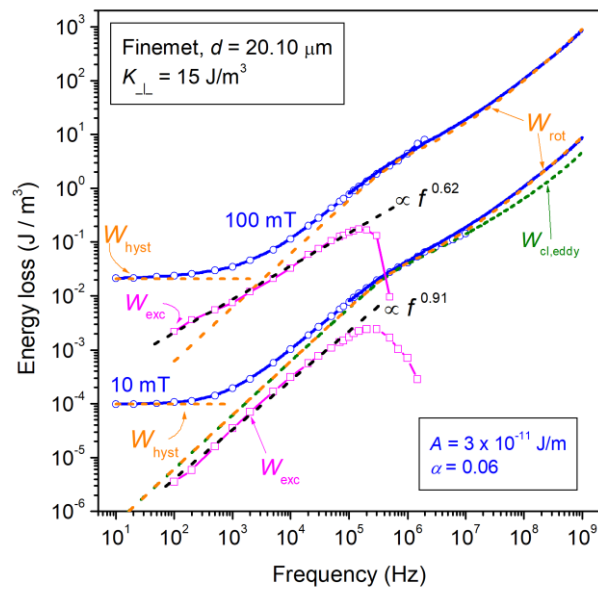


Figure 14 DC – 1GHz energy loss $W(f)$ measured in a 20.1 μm thick transverse anisotropy nanocrystalline ribbon (tapewound ring sample) with $K_{\perp} = 15 \text{ J/m}^3$ (symbols and solid lines). The loss decomposition is carried out at two different J_p values. The rotational loss $W_{\text{rot}}(f)$, calculated with Eq. (20), coincides with the measured loss beyond a few hundred kHz. **The contribution by eddy currents is put in evidence for $J_p = 10 \text{ mT}$.** The excess loss $W_{\text{exc}}(f) = W(f) - W_{\text{rot}}(f) - W_{\text{hyst}}$ obeys a power law dependence on frequency $W_{\text{exc}}(f) \propto f^p$, with $p < 1$ and decreasing with increasing J_p .